Characterizing near-surface structures at the Ostia archaeological site based on instantaneous-phase coherency inversion

Liu, Jianhuan; Ghose, Ranajit; Draganov, Deyan

DOI
10.1190/geo2021-0467.1

Publication date
2022

Document Version
Accepted author manuscript

Published in
Geophysics

GEOPHYSICS®

Characterizing near-surface structures at the Ostia archaeological site based on instantaneous-phase coherency inversion

Journal:	*Geophysics*
Manuscript ID	GEO-2021-0467.R2
Manuscript Type:	Technical Paper
Keywords:	full-waveform inversion, archaeology, Rayleigh wave, coherency, near surface
Manuscript Focus Area:	Seismic Inversion, Engineering and Environmental Geophysics

Characterizing near-surface structures at the Ostia archaeological site based on instantaneous-phase coherency inversion

Jianhuan Liu[1], Ranajit Ghose[1], Deyan Draganov[1]

[1] *Stevinweg 1, 2628 CN Delft,*

Department of Geoscience and Engineering,

Delft University of Technology

(April 5, 2022)

GEO-2020-0142

Running head: ***Instantaneous-phase coherency FWI***

ABSTRACT

Traditional least-squares full-waveform inversion (FWI) suffers from severe local minima problems in case of the presence of strongly dispersive surface waves. Additionally, recorded wavefields are often characterized by amplitude errors due to varying source coupling and incorrect 3D-to-2D geometrical-spreading correction. Thus, least-squares FWI is considered less than suitable for near-surface applications. In this paper, we introduce an amplitude-unbiased coherency measure as a misfit function that can be incorporated into FWI. Such coherency was earlier used in phase-weighted stacking (PWS) to enhance weak but coherent signals. The benefit of this amplitude-unbiased misfit function is that it can extract information uniformly for all seismic signals (surface waves, reflections, and scattered waves). Using the adjoint-state method, we show how to calculate the gradient of this new misfit function. We validate the robustness of the new approach using checkerboard tests and

synthetic data contaminated by random noise. We then apply the new FWI approach to a field dataset acquired at an archaeological site located in Ostia, Italy. The goal of this survey was to map the unexcavated archaeological remains with high-resolution. We identify a known tumulus in the FWI results. The instantaneous-phase coherency FWI results also establish that the shallow subsurface under the survey lines is quite heterogeneous. The instantaneous-phase coherency FWI of near-surface data can be a promising tool to image shallow small-scale objects buried under shallow soil covers, as found at archaeological sites.

INTRODUCTION

In recent years, 2D elastic full-waveform inversion (FWI) has evolved into a promising tool for various near-surface investigations. Tran et al. (2013) developed a 2D time-domain Gauss-Newton-based FWI and applied it for the detection of a sinkhole. The same approach has also been used in the investigation of roadway subsidence by Tran and Sperry (2018). Dokter et al. (2017) and Pan et al. (2019) applied 2D time-domain FWI to estimate a near-surface S-wave velocity structure by inverting recorded Love waves. Groos et al. (2017) applied 2D time-domain FWI to recorded shallow seismic wavefields. They successfully inverted Rayleigh waves and demonstrated the potential of 2D FWI in the reconstruction of shallow small-scale structures.

Apart from the above-mentioned examples, the field-data application of 2D FWI for near-surface prospecting is still not very common. As pointed out by Virieux and Operto (2009), one principal challenge that limits the potential application of seismic FWI to near-surface characterization is how to define the proper minimization criteria in order to reduce the sensitivity of FWI to amplitude errors. Amplitude errors might be caused by inconsistent coupling effects at different source and receiver positions (Maurer et al., 2012; Kamei et al., 2015), non-uniform source amplitudes excited at different shot locations, noise, and inaccurate 3D-to-2D correction of the geometrical-spreading effects (Forbriger et al., 2014). If the amplitude information of the recorded wavefields is not reliable, the inverted results from FWI would be questionable. Therefore, geophysicists are trying to use phase information to constrain the subsurface structures in a more stable way (Bozdağ et al., 2011; Luo et al., 2018; Mao et al., 2019; Yuan et al., 2020).

Phase information (instantaneous phase, $\phi(t)$) contains the kinematic properties of the wavefields and has a great potential to tackle the above-mentioned challenge. Fichtner et al. (2008) proposed an FWI approach based on the separation of phase and amplitude information in the time-frequency domain. By reducing the interaction between phase and amplitude, their method reduces non-linearities in FWI. Bozdağ et al. (2011) developed a similar concept but in the time domain, which avoids additional processing when compared with the time-frequency domain approach of Fichtner et al. (2008). However, the instantaneous-phase measurements involved in these approaches suffer from phase wrapping. Phase unwrapping is a challenging task, especially for noisy data (Yuan et al., 2020). To avoid the phase-wrapping problem, an alternative way is to implicitly measure the phase in the complex seismic traces. Luo et al. (2018) defined a misfit function based on the exponential phase difference ($e^{i\phi(t)}$) between observed and synthetic data. Subsequently, Yuan et al. (2020) analysed advantages and disadvantages of a misfit function based on the exponential phase difference.

In this paper, we propose a new misfit function based on the exponential phase in order to measure the coherency between measured and synthetic data. Using the theory of complex trace analysis, we show how to construct such a coherency measure from the exponential phase of the data, which is explicitly independent of the amplitude. This makes it possible to extract information uniformly for all components of seismic signals (surface waves, reflections, and scattered waves). Such a coherency measure is inspired by the concept of phase-weighted stacking (PWS) as proposed by Schimmel and Paulssen (1997) for weak but coherent signal detection. In the PWS, an amplitude-unbiased coherency is estimated from the exponential phase, which is then used to enhance the stacking of signals with similar instantaneous phase.

In the following sections, we first present the theory of FWI based on instantaneous-phase coherency. Through numerical examples, we validate the effectiveness of the new approach using checkerboard tests and synthetic data with random noise. Finally, we test our new approach on field data recorded at an archaeological site located in Ostia, Italy.

METHODOLOGY

We first describe the basic theory of the instantaneous-phase coherence, which is used to measure the similarity between two signals. After reviewing the basic theory of FWI, we present the details on how to calculate the gradient of the misfit function based on instantaneous-phase coherency using the adjoint-state method (Tarantola, 1984; Tromp et al., 2004; Plessix, 2006).

Instantaneous-phase coherence

The PWS method is an efficient technique, first proposed by Schimmel and Paulssen (1997), to reduce incoherent noise from the data. This method permits the detection of weak but coherent signals. An amplitude-unbiased coherency measure is employed to enhance components of stacked signals that share the same instantaneous phase. We extended the use of such instantaneous-phase coherency measure in a misfit function, which can be incorporated in FWI. Following the notation of Schimmel and Paulssen (1997), a complex trace $S(t)$ can be constructed by ascribing a seismic trace $s(t)$ to the real part of $S(t)$ and the Hilbert transform of $s(t)$ to the imaginary part of $S(t)$:

$$S(t) = s(t) + i\mathcal{H}\{s(t)\}. \tag{1}$$

The complex trace $S(t)$ in equation 1 can also be written in following form:

$$S(t) = A(t)e^{i\phi(t)}, \tag{2}$$

where $A(t)$ is the instantaneous amplitude which can be obtained as:

$$A(t) = \sqrt{s^2(t) + \mathcal{H}^2\{s(t)\}}, \tag{3}$$

and $\phi(t)$ is the instantaneous phase, and it can be calculated as follows:

$$\phi(t) = \arctan \frac{\mathcal{H}\{s(t)\}}{s(t)}. \tag{4}$$

However, the arc-tangent operator in equation 4 can cause a serious phase-wrapping problem (Bozdağ et al., 2011; Yuan et al., 2020). To avoid this, the instantaneous phase is implicitly estimated as:

$$e^{i\phi(t)} = \frac{S(t)}{A(t)} = \frac{s(t) + i\mathcal{H}\{s(t)\}}{\sqrt{s^2(t) + \mathcal{H}^2\{s(t)\}}}. \tag{5}$$

Schimmel and Paulssen (1997) defined the *phase stack* as a coherency measure, where amplitudes of the complex traces are not involved. The amplitude of the *phase stack* ranges between zero and one. If the instantaneous phases of all traces are perfectly coherent, then the corresponding value of the *phase stack* equals one. If the instantaneous phases of all traces vary significantly, the *phase stack* will be approximately zero.

Based on these principles and also on the phase cross-correlation concept presented in Schimmel et al. (2010), we define the following coherency measure that can be directly incorporated as a misfit function used in FWI:

$$J(t) = \frac{1}{4}\left\{\left|e^{i\phi_1(t)} - e^{i\phi_2(t)}\right|^2 - \left|e^{i\phi_1(t)} + e^{i\phi_2(t)}\right|^2\right\}, \tag{6}$$

where $\phi_1(t)$ and $\phi_2(t)$ denote the instantaneous phase of the observed and the synthetic seismic traces, respectively. In the complex plane, the amplitude of $J(t)$ can be represented by the difference (subtraction) between the length of the black vector and that of the blue vector shown in Figure 1. When two signals have significantly different instantaneous phase (Figure 1a), the amplitude of $J(t)$ has a positive value close to one. If the two signals have similar instantaneous phase (Figure 1b), the amplitude of $J(t)$ has a negative value close to minus one. Therefore, $J(t)$ can be used in FWI as a misfit function to iteratively update the model parameters till the value of $J(t)$ is minimum, which will imply that the instantaneous phases of the observed and the synthetic data are then similar.

[Figure 1 about here.]

Using the theory of complex analysis, equation 6 can also be written as

$$J(t) = \frac{1}{2}\sum_{s,r}\int_0^T \left\{\left|\sin\left(\frac{\phi_1(t) - \phi_2(t)}{2}\right)\right|^2 - \left|\cos\left(\frac{\phi_1(t) - \phi_2(t)}{2}\right)\right|^2\right\} dt, \tag{7}$$

where $\phi_1(t)$ and $\phi_2(t)$ are the instantaneous phases of the measured and the synthetic data, respectively. Note that equation 7 also suffers from local minima problem as conventional least-squares FWI. However, our misfit function mainly focuses on matching the instantaneous phase between the measured and synthetic data, which indicates that it would be robust to amplitude errors and thus it is suitable for field-data applications.

We now illustrate why our approach is robust to amplitude errors. For this purpose, we analyse Gaussian signals. In Figure 2a, the black line denotes a Gaussian signal with a peak frequency of 5 Hz, while the red dashed line represents the same Gaussian signal with 10% random noise. Figure 2b illustrates the instantaneous phase of the two signals shown in Figure 2a. Compared with the instantaneous phase of a clean Gaussian signal (black line in Figure 2b), we encounter obvious phase-wrapping effects for the noisy Gaussian signal (red dashed line in Figure 2b). Figures 2c and 2d show the real and imaginary parts of the exponentiated phase of the Gaussian signal with and without random noise, respectively. Comparing Figures 2c and 2d with Figure 2b, we notice that the exponentiated phase is more robust to random noise. Thus, the exponentiated phase makes FWI based on the instantaneous-phase coherency advantageous in handling noisy field data that contain also amplitude errors.

[Figure 2 about here.]

Overview of FWI

FWI consists of a forward-modeling step to generate the synthetic data and a nonlinear inversion process to update the model parameters by minimizing a chosen misfit function which is a measure of the difference between synthetic and recorded data. Using the adjoint-state method (Tarantola, 1984; Tromp et al., 2004; Plessix, 2006), the gradient of the misfit function with respect to the model parameters can be effectively computed through zero-lag crosscorrelation of a forward wavefield with the adjoint wavefield generated by back-propagating the residual wavefield at each receiver simultaneously. A gradient-based method, such as the nonlinear conjugate gradient (NLCG), can then be used to solve iteratively the nonlinear inverse problem.

The classic FWI formulation (Tarantola, 1984) uses the misfit function in the form of least-squares norm of the residuals between measured and synthetic data, which can be written as:

$$J_1(\mathbf{m}) = \frac{1}{2}\sum_{s,r}\int_0^T \big(d_1(\mathbf{x_s},\mathbf{x_r},t) - d_2(\mathbf{x_s},\mathbf{x_r},\mathbf{m},t)\big)^2 dt, \tag{8}$$

where $\sum_{s,r}$ represents summation over all available sources and receivers, T is the recording time, $d_1(\mathbf{x_s},\mathbf{x_r},t)$, $d_2(\mathbf{x_s},\mathbf{x_r},\mathbf{m},t)$ are, respectively, measured and synthetic data at a receiver $\mathbf{x_r}$ from a source at $\mathbf{x_s}$, and $\mathbf{m}$ denotes the model parameters. In the following, to avoid clutter, we omit the dependency of the recorded and synthetic wavefields on $\mathbf{x_s}$, $\mathbf{x_r}$, $\mathbf{m}$. The gradient of the misfit with respect to the model parameters can then be written as:

$$\delta J_1 = \sum_{s,r}\int_0^T -\big(d_1(t) - d_2(t)\big)\delta d_2(t)dt = \sum_{s,r}\int_0^T r(t)\delta d_2(t)dt, \tag{9}$$

where $\delta d_2(t)$ denotes the perturbation of the synthetic wavefield due to a model perturbation $\delta\mathbf{m}$, and $r(t)$ is the residual wavefield.

The gradient of the misfit function in equation 9 can implicitly be calculated by the adjoint-state method (Tarantola, 1984; Tromp et al., 2004), which includes the following steps: (1) forward-propagating the source wavefield, (2) back-propagating the residual wavefield, and (3) computing the zero-lag crosscorrelation of the forward-propagated and the back-propagated wavefields.

Inversion with instantaneous-phase coherency

Based on the instantaneous-phase coherence defined in equation 7, we define the following misfit function for use in FWI:

$$J_2(\mathbf{m}) = \frac{1}{4}\sum_{s,r}\int_0^T \left\{\left|e^{i\phi_1(t)} - e^{i\phi_2(t)}\right|^2 - \left|e^{i\phi_1(t)} + e^{i\phi_2(t)}\right|^2\right\} dt$$
$$= \frac{1}{4}\sum_{s,r}\int_0^T \left|\frac{d_1(t) + i\mathcal{H}\{d_1(t)\}}{\sqrt{d_1^2(t) + \mathcal{H}^2\{d_1(t)\}}} - \frac{d_2(t) + i\mathcal{H}\{d_2(t)\}}{\sqrt{d_2^2(t) + \mathcal{H}^2\{d_2(t)\}}}\right|^2 dt$$
$$- \frac{1}{4}\sum_{s,r}\int_0^T \left|\frac{d_1(t) + i\mathcal{H}\{d_1(t)\}}{\sqrt{d_1^2(t) + \mathcal{H}^2\{d_1(t)\}}} + \frac{d_2(t) + i\mathcal{H}\{d_2(t)\}}{\sqrt{d_2^2(t) + \mathcal{H}^2\{d_2(t)\}}}\right|^2 dt, \tag{10}$$

where $e^{i\phi_1(t)}$ and $e^{i\phi_2(t)}$ are the exponential phase (equation 5) of the measured and the synthetic data, respectively. The derivative of the misfit function with respect to the model parameters is expressed as (see Appendix A for details):

$$\delta J_2 = \sum_{s,r}\int_0^T \left[\frac{d_2(t)\mathcal{H}\{d_1(t)\}\mathcal{H}\{d_2(t)\}}{A_1(t)A_2^3(t)} - \frac{d_1(t)\mathcal{H}^2\{d_2(t)\}}{A_1(t)A_2^3(t)}\right]\delta d_2(t)dt$$
$$+ \sum_{s,r}\int_0^T \left[\mathcal{H}\left\{\frac{d_2^2(t)\mathcal{H}\{d_1(t)\}}{A_1(t)A_2^3(t)} - \frac{d_1(t)d_2(t)\mathcal{H}\{d_2(t)\}}{A_1(t)A_2^3(t)}\right\}\right]\delta d_2(t)dt$$
$$= \sum_{s,r}\int_0^T \tilde{r}(t)\delta d_2(t)dt. \tag{11}$$

where $A_1(t)$ and $A_2(t)$ denote the instantaneous amplitude (equation 3) of the measured and the synthetic data, respectively. The gradient in equation 11 is similar to that in equation 9 except for a different residual wavefield $\tilde{r}(t)$. To compute this new gradient, we back-propagate the residual wavefield $\tilde{r}(t)$ instead of $r(t)$, while the other steps involved in calculating the gradients are identical to the classic least-squares FWI approach described above.

SYNTHETIC TESTS

In this section, we validate the robustness of FWI based on the instantaneous-phase coherency, using checkerboard tests and synthetic data containing random noise.

Resolution test

We use checkerboard models (Figures 3a and 3b) with anomalies of different size to assess the near-surface resolution capability of FWI based on instantaneous-phase coherency. The background of these models is homogeneous, with V_P = 1000 m/s, V_S = 300 m/s and ρ = 2000 kg/m^3. We create anomalies only in the V_S model; the anomalies are such that they have ±10 % (±30 m/s) deviation from the background velocity. The checkerboard anomalies are of size 5 × 2.5 m^2 and 2.5 × 2.5 m^2 (Figures 3a and 3b). The receiver array, which is located at the surface, consists of 41 vertical geophones with a spacing of 1 m between x = 5 m and x = 45 m. During data generation, the receiver array is kept fixed whereas a vertical-force source, also deployed at the surface, moves every 2 m. The sources are located between x = 10 m and x = 40 m. With this acquisition geometry, 16 common-source gathers are computed. During the simulation, we use a band-limited spike (10 ∼ 60 Hz) as the source wavelet. For this case, the approximate resolution using Rayleigh criterion (Kallweit and Wood, 1982) can be in the range of 1.25 ∼ 7.5 m (i.e., $0.25 * 300/60 \sim 0.25 * 300/10$ m).

[Figure 3 about here.]

We perform a monoparameter inversion where only the V_S model is updated/interpreted, which is due to the fact that the dominant Rayleigh wave in the data is highly sensitive to the V_S model (Groos et al., 2017). We use the background model with $V_P = 1000$ m/s, $V_S = 300$ m/s, and $\rho = 2000$ kg/m^3 as the initial model for all inversion tests. The source wavelet is assumed to be known. A minimum of eleven iterations is performed during the inversion stage. The inversion stops once the improvement in the relative misfit change becomes smaller than 1% between two consecutive iterations (Pan et al., 2019). This also serves as a stopping criterion for other inversion tests performed in this research. The reconstructed V_S models by the instantaneous-phase coherency FWI are shown in Figures 3c and 3d. The anomalies are reconstructed very well. This illustrates the resolution capability of the instantaneous-phase coherency FWI. For the anomalies below the lateral position 10 and 40 m, there are some smearing effects caused by the limited source-receiver illumination.

Robustness to random noise

To test our FWI approach for more realistic situations, we perform inversion of synthetic data containing random noise. The V_S model is displayed in Figure 4, where two vertically separated anomalies with different velocities are present. The V_P and ρ models are set to 1000 m/s and 2000 kg/m^3, respectively. Our goal is to reconstruct these two velocity anomalies from data contaminated by different amount of random noise. The source-receiver geometry is the same as the one used in the above checkerboard tests. Also the same boundary conditions are considered on all sides. We use a band-limited spike ($10 \sim 60$ Hz) as the source wavelet. Note that the models used for the random-noise experiments are not the same as those used in the above checkerboard tests. There are some artifacts (e.g., black circle in Figure 3d) in the inverted V_S models in the checkerboard tests. If we use the models from the checkerboard tests also for the random-noise experiments, then it is hard to tell in the inverted models whether the artifacts are caused by fitting the random noise or by the

FWI algorithm. Figure 5a shows an example of a vertical component common-source gather with the source positioned at x = 18 m. A bandpass-filtered (10 $\sim$ 60 Hz) Gaussian noise is then added to the clean gathers to build two datasets with different signal-to-noise ratios (S/N=20, 10). This is done by defining the parameter `sn` in `suaddnoise` in the `Seismic Unix` open-source package (Stockwell and Cohen, 2002). Figures 5b and 5c illustrate the resulting noisy gathers.

[Figure 4 about here.]

[Figure 5 about here.]

Before we present the results of the newly proposed FWI, we show the inverted V_S models using the conventional least-squares FWI. Figures 6a, 6c, and 6e present the inverted V_S models obtained from the synthetic data in Figures 5a, 5b, and 5c, respectively. Comparing the true V_S model (Figure 4) with the FWI result shown in Figure 6a, the two velocity anomalies are well recovered by the conventional least-squares FWI when there is no noise in the data. However, when there is noise in the data, the result (Figure 6c) using conventional least-squares FWI show many undesirable artifacts. These artifacts are caused when the least-squares FWI tries to simulate the additional noise present in the data. When the amount of noise increases (S/N=10), the two vertically separated velocity anomalies become harder to recognize (Figure 6e), and the increasing presence of the artifacts becomes really problematic.

[Figure 6 about here.]

Figure 6b illustrates the inverted V_S models obtained by the instantaneous-phase coherency FWI using the noise-free shot gathers (Figure 5a). The velocity structures is imaged well even when S/N = 20 (Figure 6d). Comparing Figures 6d and 6c, the amount of artifacts is greatly reduced. When the S/N of the data decreases even further, for instance when S/N=10, we can still interpret correctly the two anomalies in the inverted result (Figure 6f). The proposed instantaneous-phase coherency FWI is robust against the presence of random noise. This is because this new approach peels off the amplitude information from the observed and the synthetic data, and tries to minimize only the instantaneous-phase coherency (instead of the residual) between them. An approach like Tikhonov regularization could potentially help such a situation, but to a limited extent.

FIELD-DATA APPLICATION

Our study area is located in the ancient Ostia, an archaeological site situated about 25 km west of Rome, Italy. Most of the ruins of Ostia were excavated in the 19th and the first half the 20th century. These ruins provide a wealth of information about the Roman urban life of antiquity. There are sill some unexcavated areas, which are mostly located at the southern boundary of the Region IV of ancient Ostia (Consoli, 2013). In 2017, we carried out a seismic survey along two lines (Ghose et al., 2020), as shown in Figure 7. Under the seismic line A, a mysterious tumulus was identified in the past and is marked by the blue dot in Figure 7. This tumulus is now covered by soil of $0.5 \sim 2$ m thickness. The goal of our survey was to characterize this buried tumulus and investigate the possible presence of other buried structures of archaeological significance.

[Figure 7 about here.]

Field-data acquisition and the main workflow

Seismic data were acquired along the two lines shown in Figure 7. Seismic energy was generated by striking vertically a metal plate with a sledgehammer. At each shot position, four vertical-force shots were excited and the recorded traces were stacked to enhance the S/N. Each shot gather consists of recorded traces from 120 vertical geophones planted at 0.25 m intervals. We used a roll-along approach to acquire the data. The receiver array is illustrated in Figure 8. In Figure 9, we summarize the main workflow for field-data application of the instantaneous-phase coherency FWI; we will give the details of each step below.

[Figure 8 about here.]

[Figure 9 about here.]

Preprocessing steps

Figures 10a and 10d display two representative common-source gathers, which are dominated by Rayleigh waves. The corresponding sources are positioned at x = 14.5 m and x = 29.5 m, respectively. The geometrical spreading of the wavefield takes place in 3D. However, 2D elastic FWI considers 2D wave propagation from a line source and 2D geometrical spreading. Therefore, a procedure that can transform the recorded point-source wavefield to its equivalent line-source wavefield is needed. We adopted the single-velocity transformation approach proposed by Forbriger et al. (2014) and Schäfer et al. (2014). This 3D-to-2D transformation is derived from a 3D Green's function but with 2D acoustic wave equation. It has been shown to perform well when applied to shallow-seismic data generated by point sources, e.g., sledgehammers (Dokter et al., 2017; Groos et al., 2017; Pan et al., 2019). This single-velocity transformation needs the following steps. First, each trace in the common-source gather is multiplied with $\sqrt{t^{-1}}$, where t is traveltime. Such a procedure corresponds to a phase shift by $\frac{\pi}{4}$. Secondly, an offset-dependent factor $F_{amp} = \sqrt{2|r|V_{ph}}$ is multiplied to each trace in order to correct their amplitudes, where V_{ph} denotes phase velocity and r is offset. We use $V_{ph} = 200$ m/s. A rough estimation of this parameter (phase velocity) is sufficient, as suggested by Groos et al. (2017).

[Figure 10 about here.]

[Figure 11 about here.]

Apart from the 3D-to-2D transformation, a few other preprocessing steps are also needed. We kill the traces within the absolute source-receiver offset of 1 m because signals in such near-offset are generally clipped (Pan et al., 2019). Dead traces are removed and all events prior to the first arrivals are muted. To mitigate the occurrence of non-casual parts in the estimated source wavelets during deconvolution, we delay the whole common-source gather by 0.01 s. Finally, we apply a bandpass filter ($5 \sim 70$ Hz) to the shot gather and normalize each trace by its maximum amplitude value. Figures 10b and 10e show the same shot gathers as in Figures 10a and 10d after the preprocessing steps described above. The same preprocessing steps are applied to all common-source gathers. Figure 11 presents the averaged frequency spectrum of the 37 preprocessed shot gathers acquired along seismic line A.

Initial models

The FWI is generally a gradient-based optimization approach, which requires a starting model in the parameter space. For simplicity, we estimate the initial model through multichannel analysis of surface waves (MASW) applied to the preprocessed data (Tran and Sperry, 2018). Figures 10c and 10f present the dispersion images calculated using slant-stacking (McMechan and Yedlin, 1981) of the data shown in Figures 10b and 10e. We can see that the energy concentrates mostly in a narrow band ($10 \sim 60$ Hz), and the phase velocities of the Rayleigh waves vary in the range 140 m/s to 160 m/s. Because V_S is slightly larger than the Rayleigh-wave phase velocity, for the starting model of V_S we consider the velocity to be changing linearly from 140 m/s at the surface to 200 m/s at the bottom of the model (z = 12.25 m). The initial V_S models for lines A and B are shown in Figures 12a and 13a, respectively. The size of the model in Figure 12a is 12.25 m in depth and 39.75 m in width (including the C-PML boundaries); the model is made of 50×160 cells with a grid spacing of 0.25 m. The depth of the model is determined approximately by $1/2 \sim 1/3$ of the length of the receiver array ($29.75/3 \sim 29.75/2$ m). The initial V_P model is calculated from the initial V_S model assuming a Possion's ratio of 0.3. The density is kept constant at 2000 km/m^3 during the inversion. We do not invert for density because the density of the subsurface has a relatively small impact on the energy of the recorded wavefield at the surface (Groos et al., 2017) and our primary goal is to get a good V_S model. To account for the strong attenuation effects in the near-surface, we use a constant quality factor ($Q_S = Q_P = 15$) to simulate the viscoelastic wave propagation. These optimal Q values are determined by repeating the inversion for a set of constant quality factors and examining the misfit between the field data and the synthetic data (Dokter et al., 2017).

FWI strategies

With the initial models for lines A and B described above, we start the instantaneous-phase coherency FWI by first inverting data in the frequency bandwidth 5 $\sim$ 10 Hz. The upper corner frequency of the bandpass filter is then progressively increased to 20, 30, 40, 50, 60 Hz (Bunks et al., 1995). The FWI result obtained in each frequency band becomes the initial model for inversion in the next frequency band. We move to the next frequency band when the relative misfit value at an iteration becomes less than 1% compared to the misfit value in the previous iteration. During the inversion, we update the V_S and V_P models independently, while the density model is kept fixed. We use a parabolic line search method (Nocedal and Wright, 2006) to determine the optimum step length for updating the V_P and V_S models. As we can see in the recorded shot gathers (e.g., Figures 10a and 10d), the amplitude of the P-waves is much smaller than that of the Rayleigh waves. The V_P model is thus not as well constrained as the V_S model. Therefore, we only show and interpret the inverted V_S models (Groos et al., 2017). To update the models in the shallow parts, we apply a preconditioning, semicircular taper to the gradient of each shot. We also smooth the gradients using a 2D Gaussian filter (Ravaut et al., 2004) with a length of approximately half of the dominant wavelength in order to avoid the occurrence of small-scale artifacts below the FWI resolution limit. For the two seismic lines, the instantaneous-phase coherency FWI converges to provide the V_S models shown in Figures 12b and 13b.

[Figure 12 about here.]

[Figure 13 about here.]

FWI results and their interpretations

In absence of ground truth, we evaluate the final inverted models (Figures 12b and 13b) from their ability to explain the measured seismic wavefields. We compute synthetic shot gathers using the source wavelets estimated by a stabilised Wiener deconvolution method (Köhn et al., 2016). The basic idea behind this approach is to deconvolve the recorded data using simulated data obtained from the current subsurface model. In Figures 14 and 15, we show comparisons between measured shot gathers and synthetic shot gathers for seismic line A and B, respectively. The main events in the observed common-source gather (e.g., black lines in Figure 14a) and the corresponding synthetic gather (e.g., red lines in Figure 14a) are very similar. From the overlay of these two gathers (e.g., Figure 14a), we can see that the main events match very well without any cycle skipping. There are also some realistic events that are not fully matched. This phenomenon is expected because our misfit function (equation 7) is mainly designed to match the instantaneous-phase part of the measured and synthetic data. To recover amplitude information in the synthetic data, we also perform a subsequent envelope-based FWI, starting from the inverted models in Figures 12a and 13a. However, in the final inverted models, no significant velocity changes are observed, which means that our final inverted models (Figures 12b and 13b) are good enough to represent the subsurface given the data. Figure 16 shows a comparison between the preprocessed field data, synthetic data from the initial models, and synthetic data from the inverted models in the phase velocity-frequency domain. In the Rayleigh-wave dispersion images of the preprocessed data (e.g., Figure 16a), we can observe fundamental and first higher modes. Compared with the dispersion image of the synthetic data obtained from the initial models, the dispersion image from the synthetic data derived from the inverted models is able to improve the fitting of both the fundamental and first higher modes.

[Figure 14 about here.]

[Figure 15 about here.]

[Figure 16 about here.]

The good fit between the observed and the synthetic data offers confidence to the inverted, final V_S models. For the seismic line A, the 2D V_S profile obtained from instantaneous-phase coherency FWI (Figure 12b) shows a low-velocity area at x = $15 \sim 20$ m (black ellipse in Figure 12b). A known tumulus of archaeological significance, which is covered by soft soil of thickness $0.5 \sim 2$ m, was identified in the same vicinity (Ghose et al., 2020). Based on this information, we interpret the very shallow low-velocity area in our FWI result as the anticipated tumulus body. In the final V_S models for the seismic line B, we notice the presence of many small-size anomalies. Some of these have been marked by black arrows in Figure 13b. At present it is unknown whether these heterogeneities correspond to archaeological objects. Recent shear-wave reflection studies also suggest possible presence of multiple buried structures in this part of the field (Ghose et al., 2020).

Ghose et al. (2020) analysed S-wave vibrator data acquired along the same two lines in Ostia. The acquisition geometry is similar to that shown in Figure 8. We overlay the stacked seismic reflection sections from Ghose et al. (2020) and the inverted V_S profiles from our FWI (Figures 12c and 13c). The location of the body-wave scatterers mapped in the stacked sections matches with the locations of some of the plausible underground objects imaged in our FWI results. Distinct, shallow diffraction events were identified in the raw S-wave data. There are also many structures visible in the inverted V_S models that are hard to interpret. Quantifying the uncertainties can help the final interpretation of the

FWI results. Uncertainties present in the inverted models can be comming from: (1) the non-linearity of FWI, (2) the uncertainties in building the starting models, (3) the selection of frequency bandwidth for each inversion stage, and (4) undesired amplitude variations at each source/receiver position. Resolution analysis (Fichtner and Trampert, 2011; Cai and Zelt, 2019) is a promising tool for the quantification of such uncertainties; this needs further investigations.

The field data acquired in 2D seismic surveys are often contaminated by scattered waves from the out-of-plane objects and other incoherent noise. There are ancient walls (Figure 7) near our survey lines. The seismic lines were planned in such a way that the distance from these walls to the seismic line is more than $10 \sim 12$ m. Therefore, the very shallow scattered energy in our data is most probably not due to side-scatterring. Nevertheless, it is possible that the side-scattering from those ancients walls is present at slightly later times in the acquired seismic wavefield. For a reliable interpretation, one should try to eliminate such events before performing FWI. Seismic interferometry can be advantageously used to retrieve and enhance the surface waves arriving from the inline direction (Liu et al., 2018; Balestrini et al., 2019; Liu et al., 2021) and suppress the interference of out-of-plane seismic energy. Inversion of such retrieved data can prevent imaging artifacts. 3D seismic imaging can also add more constraints to such interpretation. This will be the direction of our future research.

CONCLUSION

We introduced a new instantaneous-phase coherency measure, and extend it as a misfit function that can be directly incorporated into full-waveform inversion (FWI). Such instantaneous-phase coherency has been a key to the phase-weighted stacking for enhancing signals with similar instantaneous phase. We presented the details of how to compute the gradients of a new misfit function using the adjoint-state method. We validated the robustness of our FWI approach using checkerboard tests and data contaminated by random noise. Finally, we applied our new approach to field data acquired at an archaeological site located in Ostia, Italy. The locality containing a tumulus, known to be buried under a shallow soil cover, could be identified in our FWI results. The inversion results of instantaneous-phase coherency FWI also showed that the subsurface of this unexcavated part of the archaeological site of Ostia has a high degree of heterogeneity, with the likely presence of small objects in the shallow subsurface. But this interpretation needs more careful analysis. Our results suggest that FWI based on the instantaneous-phase coherency method can be a promising noninvasive tool for archaeological site investigation.

APPENDIX A

GRADIENT FOR INSTANTANEOUS-PHASE COHERENCE

The gradient of the misfit function based on the exponential phase ($e^{i\phi}$) difference is given in Luo et al. (2018) and Yuan et al. (2020). Our new misfit function utilizes the exponential phase to measure the coherency between the recorded and the synthetic data. Following these earlier works, we give details on how to derive the gradient of the misfit defined in equation 10 with respect to model parameters $\mathbf{m}$.

The instantaneous-phase coherence misfit function defined in equation 10 can be expanded as:

$$
\begin{aligned}
J_2(\mathbf{m}) &= \frac{1}{4}\sum_{s,r}\int_0^T \left\{ \left| e^{i\phi_1(t)} - e^{i\phi_2(t)} \right|^2 - \left| e^{i\phi_1(t)} + e^{i\phi_2(t)} \right|^2 \right\} dt \\
&= \frac{1}{4}\sum_{s,r}\int_0^T \left| \frac{d_1(t) + i\mathcal{H}\{d_1(t)\}}{A_1(t))} - \frac{d_2(t) + i\mathcal{H}\{d_2(t)\}}{A_2(t))} \right|^2 dt \\
&- \frac{1}{4}\sum_{s,r}\int_0^T \left| \frac{d_1(t) + i\mathcal{H}\{d_1(t)\}}{A_1(t))} + \frac{d_2(t) + i\mathcal{H}\{d_2(t)\}}{A_2(t))} \right|^2 dt \\
&= \frac{1}{4}\sum_{s,r}\int_0^T \left\{ \left| \frac{d_1(t)}{A_1(t)} - \frac{d_2(t)}{A_2(t))} \right|^2 + \left| \frac{\mathcal{H}\{d_1(t)\}}{A_1(t)} - \frac{\mathcal{H}\{d_2(t)\}}{A_2(t)} \right|^2 \right\} dt \\
&- \frac{1}{4}\sum_{s,r}\int_0^T \left\{ \left| \frac{d_1(t)}{A_1(t)} + \frac{d_2(t)}{A_2(t))} \right|^2 + \left| \frac{\mathcal{H}\{d_1(t)\}}{A_1(t)} + \frac{\mathcal{H}\{d_2(t)\}}{A_2(t)} \right|^2 \right\} dt.
\end{aligned}
\tag{A-1}
$$

To simplify this expression, $R_1(t)$, $I_1(t)$, $R_2(t)$, $I_2(t)$ can be introduced as follows:

$$
\begin{cases}
R_1(t) = \frac{d_1(t)}{A_1(t)} - \frac{d_2(t)}{A_2(t))}, \quad I_1(t) = \frac{\mathcal{H}\{d_1(t)\}}{A_1(t)} - \frac{\mathcal{H}\{d_2(t)\}}{A_2(t)}; \\
R_2(t) = \frac{d_1(t)}{A_1(t)} + \frac{d_2(t)}{A_2(t))}, \quad I_2(t) = \frac{\mathcal{H}\{d_1(t)\}}{A_1(t)} + \frac{\mathcal{H}\{d_2(t)\}}{A_2(t)}.
\end{cases}
\tag{A-2}
$$

Equation A-1 can be further simplified to:

$$
J_2(\mathbf{m}) = \frac{1}{4}\sum_{s,r}\int_0^T \left\{ R_1^2(t) + I_1^2(t) - R_2^2(t) - I_2^2(t) \right\} dt.
\tag{A-3}
$$

The derivative of the misfit function defined in equation A-3 can be written as:

$$
\delta J_2 = \frac{1}{2}\sum_{s,r}\int_0^T \left\{ R_1(t)\delta R_1(t) + I_1(t)\delta I_1(t) - R_2(t)\delta R_2(t) - I_2(t)\delta I_2(t) \right\} dt.
\tag{A-4}
$$

Note that:

$$
\begin{cases}
\delta R_2(t) = -\delta R_1(t) = \delta\left(\frac{d_2(t)}{A_2(t)}\right); \\
\delta I_2(t) = -\delta I_1(t) = \delta\left(\frac{\mathcal{H}\{d_2(t)\}}{A_2(t)}\right).
\end{cases}
\tag{A-5}
$$

Substituting equation A-5 into equation A-4, we get:

$$\delta J_2 = -\sum_{s,r}\int_0^T \left\{ \frac{d_1(t)}{A_1(t)}\delta\Big(\frac{d_2(t)}{A_2(t)}\Big) + \frac{\mathcal{H}\{d_1(t)\}}{A_1(t)}\delta\Big(\frac{\mathcal{H}\{d_2(t)\}}{A_2(t)}\Big)\right\} dt. \tag{A-6}$$

Next, we present the details on how to evaluate $\delta\Big(\frac{d_2(t)}{A_2(t)}\Big)$ and $\delta\Big(\frac{\mathcal{H}\{d_2(t)\}}{A_2(t)}\Big)$:

$$\begin{aligned}\delta\Big(\frac{d_2(t)}{A_2(t)}\Big) &= \delta\Big(\frac{d_2(t)}{\sqrt{d_2^2(t)+\mathcal{H}^2\{d_2(t)\}}}\Big)\\ &= \frac{\delta d_2(t)\sqrt{d_2^2(t)+\mathcal{H}^2\{d_2(t)\}}}{d_2^2(t)+\mathcal{H}^2\{d_2(t)\}} - \frac{\delta d_2(t) d_2^2(t) + d_2(t)\mathcal{H}\{d_2(t)\}\delta(\mathcal{H}\{d_2(t)\})}{\Big[d_2^2(t)+\mathcal{H}^2\{d_2(t)\}\Big]^{\frac{3}{2}}}\\ &= \frac{\delta d_2(t)\mathcal{H}^2\{d_2(t)\} - d_2(t)\mathcal{H}\{d_2(t)\}\delta(\mathcal{H}\{d_2(t)\})}{\Big[d_2^2(t)+\mathcal{H}^2\{d_2(t)\}\Big]^{\frac{3}{2}}}.\end{aligned} \tag{A-7}$$

Here, we make use of two properties of the Hilbert transform, as also presented in Yuan et al. (2015):

$$\begin{cases} \delta\mathcal{H}\{d_2(t)\} = \mathcal{H}\{\delta d_2(t)\};\\ \big\langle\mathcal{H}\{d_1(t)\}, d_2(t)\big\rangle = -\big\langle d_1(t), \mathcal{H}\{d_2(t)\}\big\rangle. \end{cases} \tag{A-8}$$

Thus, the second part of the numerator in equation A-7 can be rewritten as:

$$\begin{aligned} d_2(t)\mathcal{H}\{d_2(t)\}\delta(\mathcal{H}\{d_2(t)\}) &= d_2(t)\mathcal{H}\{d_2(t)\}\mathcal{H}\{\delta d_2(t)\}\\ &= -\mathcal{H}\Big\{d_2(t)\mathcal{H}\{d_2(t)\}\Big\}\delta d_2(t). \end{aligned} \tag{A-9}$$

Substituting equation A-9 into equation A-7, we get:

$$\delta\Big(\frac{d_2(t)}{A_2(t)}\Big) = \frac{\mathcal{H}^2\{d_2(t)\} + \mathcal{H}\Big\{d_2(t)\mathcal{H}\{d_2(t)\}\Big\}}{\Big[d_2^2(t)+\mathcal{H}^2\{d_2(t)\}\Big]^{\frac{3}{2}}}\delta d_2(t). \tag{A-10}$$

Similarity, $\delta\Big(\frac{\mathcal{H}\{d_2(t)\}}{A_2(t)}\Big)$ can be obtained as

$$\delta\Big(\frac{\mathcal{H}\{d_2(t)\}}{A_2(t)}\Big) = \frac{-\mathcal{H}\{d_2^2(t)\} - d_2(t)\mathcal{H}\{d_2(t)\}}{\Big[d_2^2(t) + \mathcal{H}^2\{d_2(t)\}\Big]^{\frac{3}{2}}}\delta d_2(t). \tag{A-11}$$

Substituting equation A-10 and A-11 into equation A-6, and rearranging the orders, we have the gradient of the misfit function defined in equation 10 as

$$\begin{aligned}\delta J_2 = &\sum_{s,r}\int_0^T \left[\frac{d_2(t)\mathcal{H}\{d_1(t)\}\mathcal{H}\{d_2(t)\}}{A_1(t)A_2^3(t)} - \frac{d_1(t)\mathcal{H}^2\{d_2(t)\}}{A_1(t)A_2^3(t)}\right]\delta d_2(t)dt \\ &+ \sum_{s,r}\int_0^T \left[\mathcal{H}\left\{\frac{d_2^2(t)\mathcal{H}\{d_1(t)\}}{A_1(t)A_2^3(t)} - \frac{d_1(t)d_2(t)\mathcal{H}\{d_2(t)\}}{A_1(t)A_2^3(t)}\right\}\right]\delta d_2(t)dt.\end{aligned} \tag{A-12}$$

REFERENCES

Balestrini, F., D. Draganov, A. Malehmir, P. Marsden, and R. Ghose, 2019, Improved target illumination at Ludvika mines of Sweden through seismic-interferometric surface-wave suppression: Geophysical Prospecting, **68**, 200–213.

Bozdağ, E., J. Trampert, and J. Tromp, 2011, Misfit functions for full waveform inversion based on instantaneous phase and envelope measurements: Geophysical Journal International, **185**, 845–870.

Bunks, C., F. M. Saleck, S. Zaleski, and G. Chavent, 1995, Multiscale seismic waveform inversion: Geophysics, **60**, 1457–1473.

Cai, A., and C. A. Zelt, 2019, Data weighted full-waveform inversion with adaptive moment estimation for near-surface seismic refraction data: 89th Annual International Meeting, SEG, Expanded Abstracts, 2858–2862.

Consoli, R. H., 2013, World history encyclopedia: Ostia, www.worldhistory.org/ostia, accessed 3 March 2022.

Dokter, E., D. Köhn, D. Wilken, D. D. Nil, and W. Rabbel, 2017, Full waveform inversion of SH- and Love-wave data in near-surface prospecting: Geophysical Prospecting, **65**, 216–236.

Fichtner, A., B. L. N. Kennett, H. Igel, and H.-P. Bunge, 2008, Theoretical background for continental- and global-scale full-waveform inversion in the time-frequency domain: Geophysical Journal International, **175**, 665–685.

Fichtner, A., and J. Trampert, 2011, Resolution analysis in full waveform inversion: Geophysical Journal International, **187**, 1604–1624.

Forbriger, T., L. Groos, and M. Schäfer, 2014, Line-source simulation for shallow-seismic data. Part 1: theoretical background: Geophysical Journal International, **198**, 1387–1404.

Ghose, R., J. Liu, D. Draganov, D. Ngan-Tillard, M. Warnaar, J. Brackenhoff, J. van den Berg, and H. Stoger, 2020, Ultra-shallow shear-wave reflections locating near-surface buried structures in the unexcavated southern fringe of the ancient Ostia, Rome, *in* H. Kamermans, L. Bouke van der Meer, eds., Designating Place: archaeological perspectives on built environments in Ostia and Pompeii: Archaeological Studies Leiden University (ASLU) 50, 51–62.

Groos, L., M. Schäfer, T. Forbriger, and T. Bohlen, 2017, Application of a complete workflow for 2D elastic full-waveform inversion to recorded shallow-seismic Rayleigh waves: Geophysics, **82**, no. 2, R109–R117.

Kallweit, R. S., and L. C. Wood, 1982, The limits of resolution of zero-phase wavelets: Geophysics, **47**, 1035–1046.

Kamei, R., T. Miyoshi, R. G. Pratt, M. Takanashi, and S. Masaya, 2015, Application of waveform tomography to a crooked-line 2D land seismic data set: Geophysics, **80**, no. 5, B115–B129.

Köhn, D., T. Meier, M. Fehr, D. D. Nil, and M. Auras, 2016, Application of 2D elastic Rayleigh waveform inversion to ultrasonic laboratory and field data: Near Surface Geophysics, **14**, 461–467.

Liu, J., D. Draganov, and R. Ghose, 2018, Seismic interferometry facilitating the imaging of shallow shear-wave reflections hidden beneath surface waves: Near Surface Geophysics, **16**, 372–382.

Liu, J., D. Draganov, R. Ghose, and Q. Bourgeois, 2021, Near-surface diffractor detection at archaeological sites based on an interferometric workflow: Geophysics, **86**, no. 3, WB1–WB11.

Luo, J., R.-S. Wu, and F. Gao, 2018, Time-domain full waveform inversion using instantaneous phase information with damping: Journal of Geophysics and Engineering, **15**, 1032–1041.

Mao, J., J. Sheng, and G. Hilburn, 2019, Phase only reflection full-waveform inversion for high resolution model update: 89th Annual International Meeting, SEG, Expanded Abstracts, 1305–1309.

Maurer, H., S. A. Greenhalgh, E. Manukyan, S. Marelli, and A. G. Green, 2012, Receiver-coupling effects in seismic waveform inversions: Geophysics, **77**, no. 1, R57–R63.

McMechan, G. A., and M. J. Yedlin, 1981, Analysis of dispersive waves by wave field transformation: Geophysics, **46**, 869–874.

Nocedal, J., and S. Wright, 2006, Numerical optimization: Springer Science & Business Media.

Pan, Y., L. Gao, and T. Bohlen, 2019, High-resolution characterization of near-surface structures by surface-wave inversions: From dispersion curve to full waveform: Surveys in Geophysics, **40**, 167–195.

Plessix, R.-E., 2006, A review of the adjoint-state method for computing the gradient of a functional with geophysical applications: Geophysical Journal International, **167**, 495–503.

Ravaut, C., S. Operto, L. Improta, J. Virieux, A. Herrero, and P. Dell'Aversana, 2004, Multiscale imaging of complex structures from multifold wide-aperture seismic data by frequency-domain full-waveform tomography: application to a thrust belt: Geophysical Journal International, **159**, 1032–1056.

Schimmel, M., and H. Paulssen, 1997, Noise reduction and detection of weak, coherent signals through phase-weighted stacks: Geophysical Journal International, **130**, 497–505.

Schimmel, M., E. Stutzmann, and J. Gallart, 2010, Using instantaneous phase coherence for signal extraction from ambient noise data at a local to a global scale: Geophysical Journal International, **184**, 494–506.

Schäfer, M., L. Groos, T. Forbriger, and T. Bohlen, 2014, Line-source simulation for shallow-seismic data. Part 2: full-waveform inversion—a synthetic 2-D case study: Geophysical Journal International, **198**, 1405–1418.

Stockwell, J., and J. K. Cohen, 2002, The new SU user's manual: Center for Wave Phenomena, Colorado School of Mines, Golden, USA, **3**.

Tarantola, A., 1984, Inversion of seismic reflection data in the acoustic approximation: Geophysics, **49**, 1259–1266.

Tran, K. T., M. McVay, M. Faraone, and D. Horhota, 2013, Sinkhole detection using 2D full seismic waveform tomography: Geophysics, **78**, no. 5, R175–R183.

Tran, K. T., and J. Sperry, 2018, Application of 2D full-waveform tomography on land-streamer data for assessment of roadway subsidence: Geophysics, **83**, no. 3, EN1–EN11.

Tromp, J., C. Tape, and Q. Liu, 2004, Seismic tomography, adjoint methods, time reversal and banana-doughnut kernels: Geophysical Journal International, **160**, 195–216.

Virieux, J., and S. Operto, 2009, An overview of full-waveform inversion in exploration geophysics: Geophysics, **74**, no. 6, WCC1–WCC26.

Yuan, Y. O., E. Bozdağ, C. Ciardelli, F. Gao, and F. J. Simons, 2020, The exponentiated phase measurement, and objective-function hybridization for adjoint waveform tomography: Geophysical Journal International, **221**, 1145–1164.

Yuan, Y. O., F. J. Simons, and E. Bozdağ, 2015, Multiscale adjoint waveform tomography for surface and body waves: Geophysics, **80**, no. 5, R281–R302.

LIST OF FIGURES

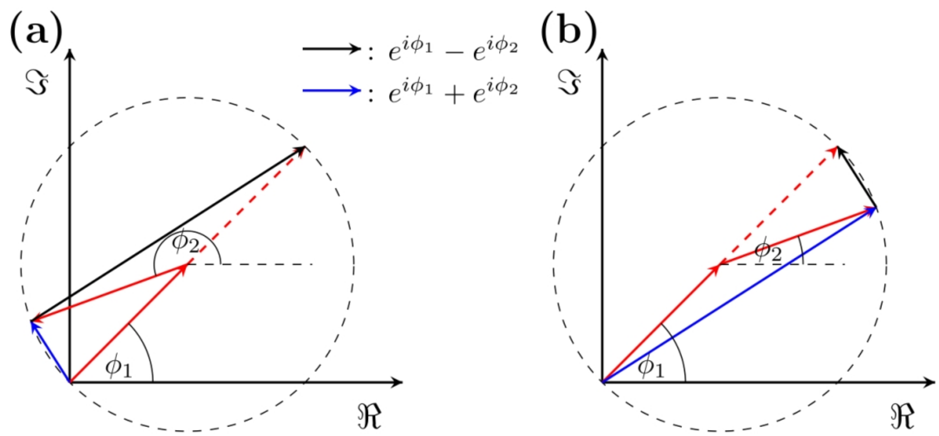

Figure 01: Illustrations of instantaneous-phase coherency as defined in equation 7. The red arrows denotes $e^{i\phi_1}$ and $e^{i\phi_2}$, whereas the black and blue arrows represent $e^{i\phi_1}-e^{i\phi_2}$ and $e^{i\phi_1}+e^{i\phi_2}$, respectively. The black arrow measures how the instantaneous phases of two signals are close to each other, while the blue arrow measures how much the instantaneous phases of two signals differ from 180 degrees. Either of the two measurements can be used on its own as a misfit function of FWI by matching the instantaneous phase between the measured and the synthetic data. Using numerical experiments (not shown in this paper), we found that the performance of different misfit functions (black arrow, blue arrow, combination of black and blue arrows) is quite similar. The reason why we design a misfit function with a combination of black and blue arrows is that this approach is novel and it has the chance to be more robust to noise. $J(t)$ is obtained by subtracting the square of the two vectors given by the black and the blue arrows. (a) When the two signals have significantly different instantaneous phases, $J (t)$ {will} be close to 1. (b) When the two signals have similar instantaneous phases, $J(t)$ will be close to -1.

305x150mm (118 x 118 DPI)

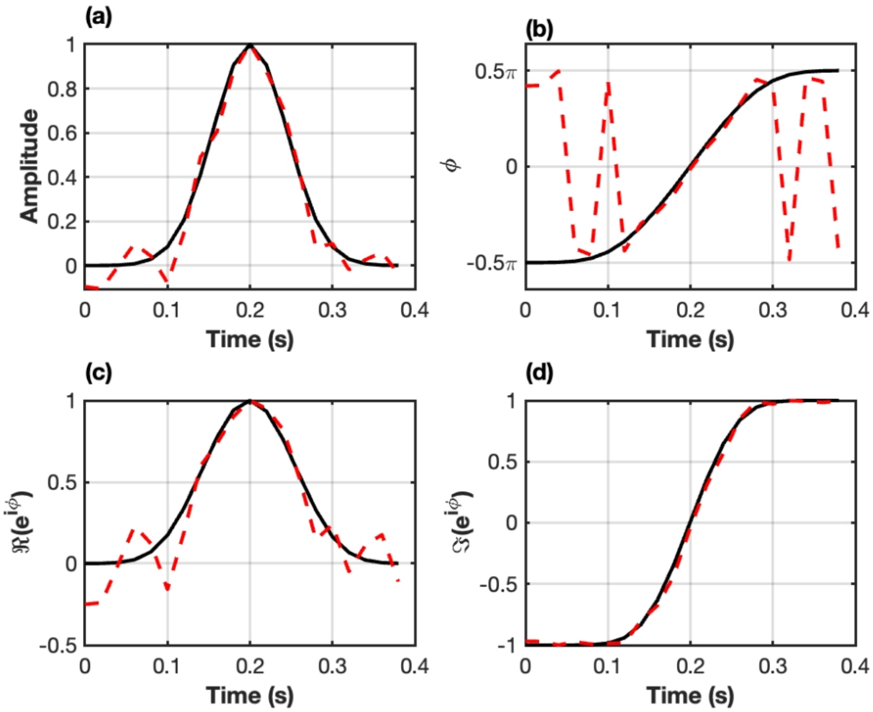

Figure 02: A simple synthetic example to demonstrate the robustness to noise of instantaneous phase ($\phi(t)$) and exponentiated phase ($e^{i\phi(t)}$). (a) A Gaussian signal with a peak frequency of 5 Hz (black line) and the same Gaussian signal with random noise and S/N = 10 (red-dashed line). In (b), (c), (d), we use black and red-dashed lines to represent respectively the instantaneous phase and exponentiated phase of the two signals presented in (a). (b) The instantaneous phase of the two signals as presented in (a). Note that for the signal with random noise, there are marked phase jumps. (c) The real part of the exponentiated phase of the two signals presented in (a). (d) The imaginary part of the exponentiated phase of the two signals presented in (a). Comparing (c), (d) with (b), it is clear that the exponentiated phase is more robust to noise.

502x376mm (59 x 59 DPI)

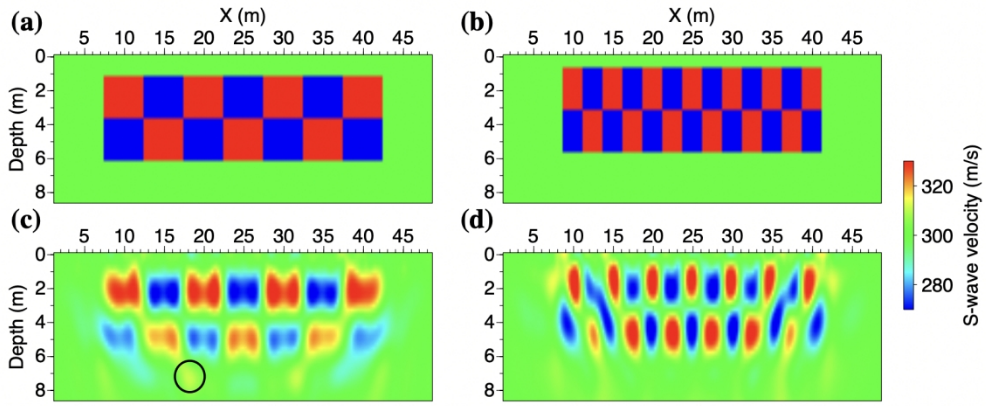

Figure 03: Checkerboard tests for resolution analysis. (a) True V_S model containing velocity anomalies. The size of these anomalies is $5 \times 2.5~m^2$; (c) the result of instantaneous-phase coherency FWI. (b), (d) the same as in (a), (c) but for anomalies with size of $2.5 \times 2.5~m^2$. A homogeneous background ($V_S = 300~m/s$) is used in all tests. The black circle indicates an artifact caused by the FWI algorithm.

318x135mm (144 x 144 DPI)

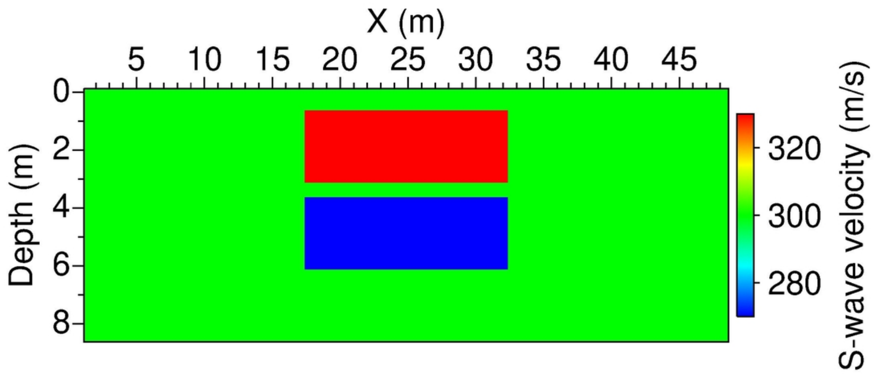

Figure 04: A simple V_S model used to test the robustness of the instantaneous-phase coherency FWI to random noise.

105x49mm (300 x 300 DPI)

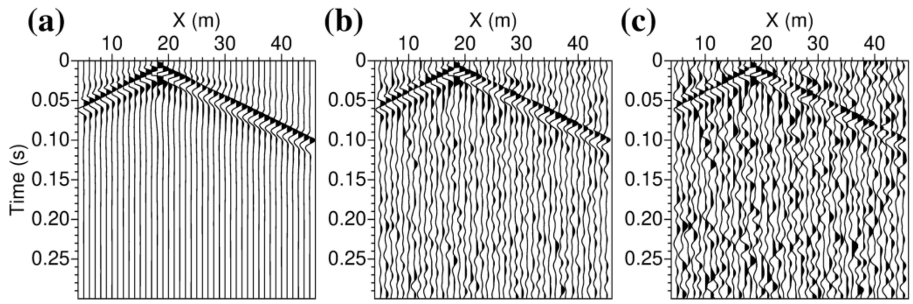

Figure 05: (a) Common-source gather (vertical receiver component) computed for the model shown in Figure~4}, where the source is positioned at x = 18 m; (b) the same as (a) but with random noise of S/N = 20 added; (c) the same as (a) but with random noise of S/N = 10 added.

214x80mm (300 x 300 DPI)

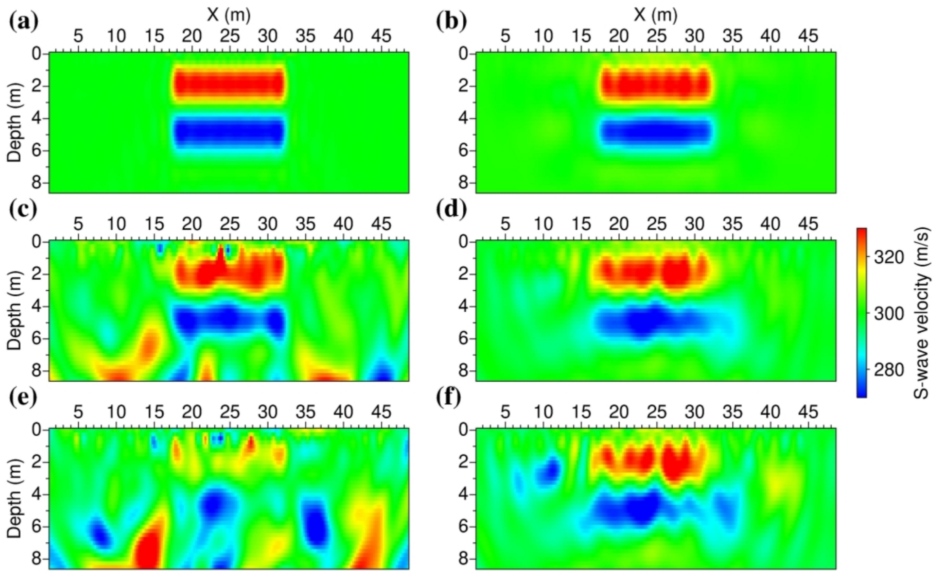

Figure 06: Test of inversion robustness to random noise present in the data. To maintain consistency with the checkerboard tests illustrated in Figure 3, the same bandpass filter (10 to 60~Hz) is applied to the data in Figure 5. (a) Inverted V_S model by least-squares FWI using noise-free synthetic data; (c) the same as (a) but for data contaminated by random noise with S/N = 20; (e) the same as (a) but for data contaminated by random noise with S/N = 10. (b), (d), (f) are the same as (a), (c), (e), respectively, but using instantaneous-phase coherency FWI.

189x120mm (300 x 300 DPI)

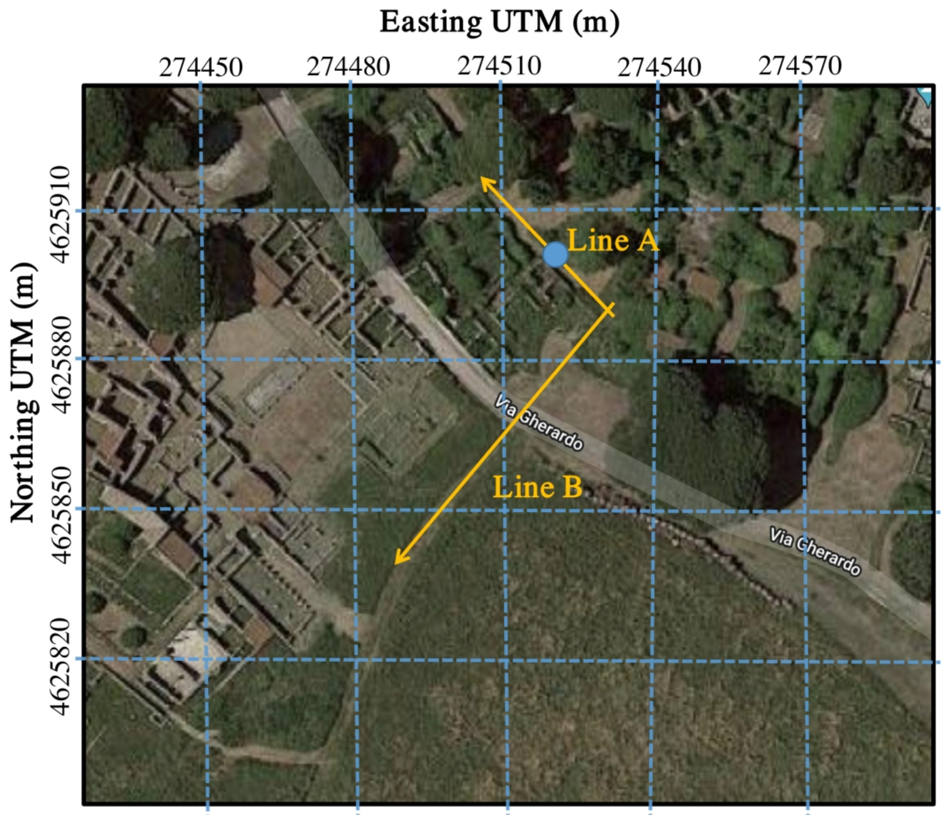

Figure 07: Photo of an unexcavated area in the ancient Ostia (from Google map). The two seismic lines A and B are indicated by yellow lines, where the arrows point in the direction of increasing coordinates (directions in which the source was moved) along the x-axes \cite[]{Ghose_2020}. The blue dot marks the approximate location of a tumulus identified earlier. Note that there are ancient walls present not too far away from the seismic lines.

508x432mm (118 x 118 DPI)

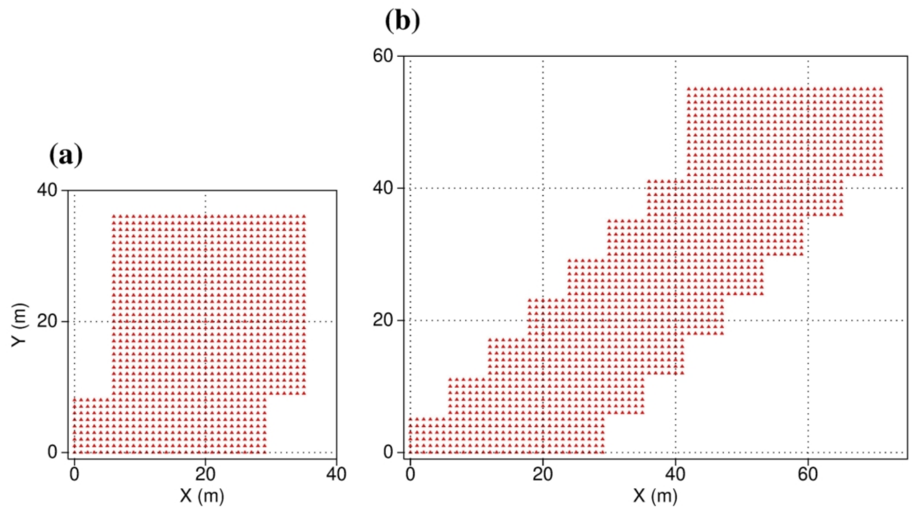

Figure 08: Layout of the receiver arrays used to acquire 2D seismic data along (a) seismic line A and (b) seismic line B, marked in Figure 7. For seismic lines A and B, the receiver interval is 0.25 m, while the source interval is 1 m. The number of common-source gathers acquired along seismic lines A and B are 37 and 57, respectively. The x-axis denotes the lateral positions of receivers, the y-axis represents the corresponding source positions for each receiver. The small, red triangles represent vertical, single-component geophones. Every fourth receiver position is displayed here.

189x102mm (300 x 300 DPI)

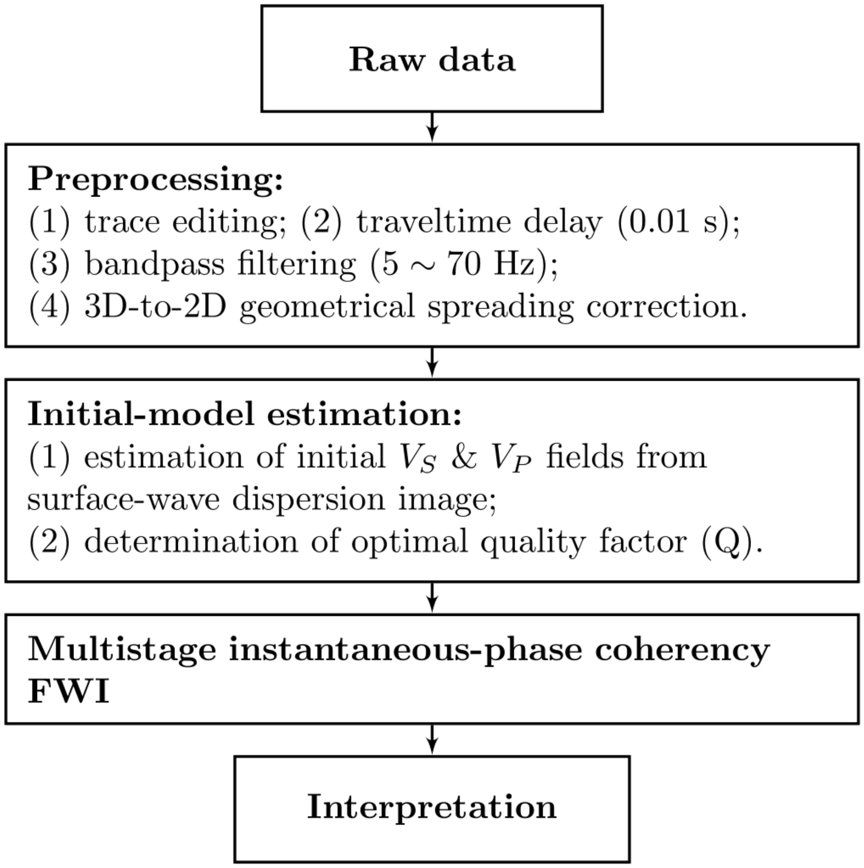

Figure 09: Workflow for field-data application of the instantaneous-phase coherency FWI.

253x241mm (118 x 118 DPI)

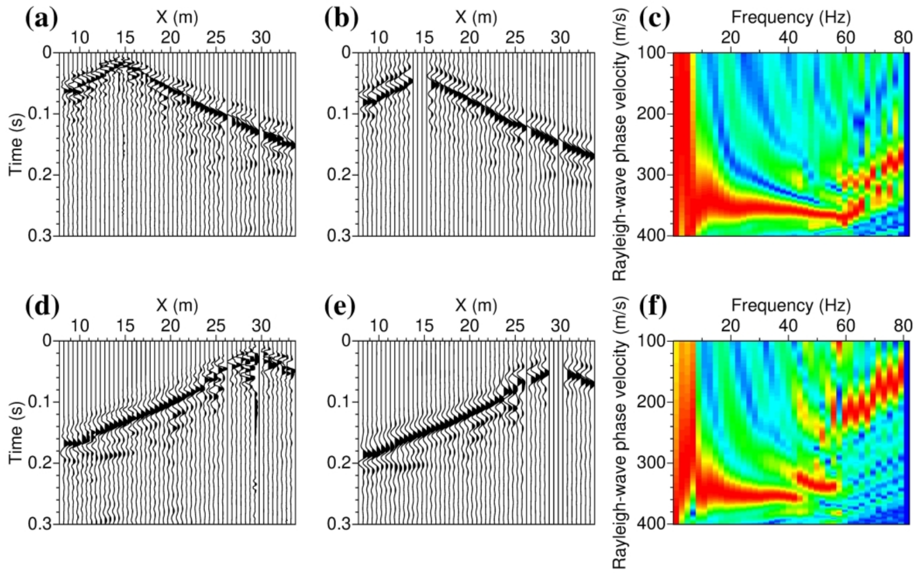

Figure 10: (a) Muted common-source gather along with seismic line A, where the source is positioned at x = 14.5 m; (b) the same as (a) but after preprocessing described in the text; (c) Rayleigh-wave dispersion image obtained by slant-stacking of the preprocessed shot gather shown in (b). (d), (e), (f) are respectively same as (a), (b), (c) but for a common-source gather where the source located at x = 29.5 m.

241x143mm (300 x 300 DPI)

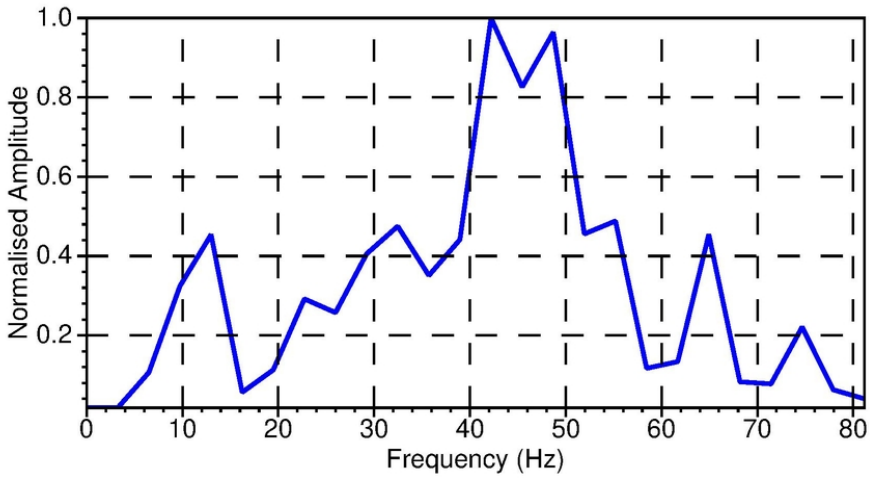

Figure 11: Average amplitude spectrum of 37 preprocessed shot gathers acquired along with seismic line A.

81x51mm (300 x 300 DPI)

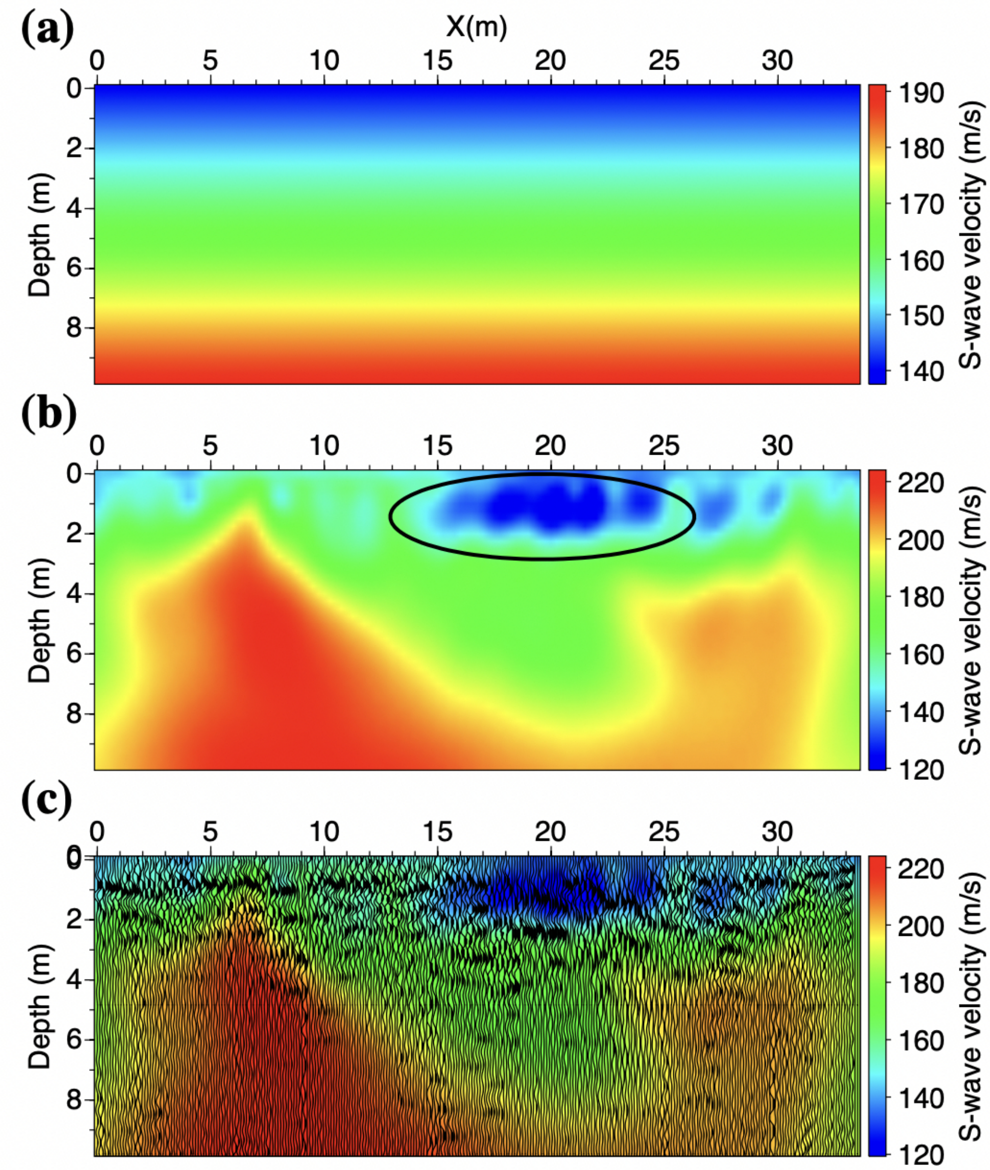

Figure 12: Inverted V_S model for seismic line A. (a) Initial model used in inversion; (b) result of instantaneous-phase coherency FWI after the 6th stage of sequential inversion (i.e., frequency band $5 \sim 60$ Hz); (c) the overlay of CMP stacked section from S-wave reflection data \cite[]{Ghose_2020} and the inverted V_S model shown in (b). The ellipse in (b) marks the area where a tumulus was previously identified

183x218mm (144 x 144 DPI)

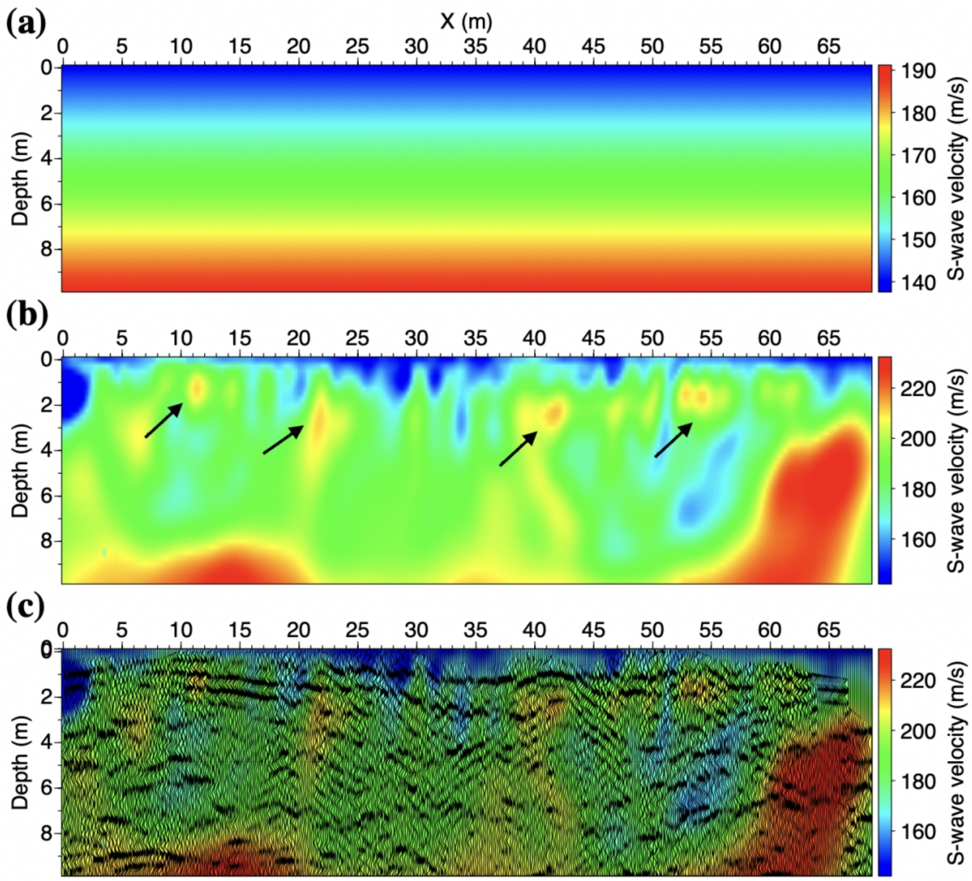

Figure 13: Inverted \$V_S\$ model for seismic line B. (a) Initial model used in inversion; (b) result of instantaneous-phase coherency FWI after the 6th stage of sequential inversion (i.e., frequency band \$5 \sim 60\$ Hz); (c) the overlay of the CMP stacked section from S-wave reflection data \cite[]{Ghose_2020} and the inverted \$V_S\$ model presented in (d). The black arrows in (b) indicate potential subsurface heterogeneities of interest.

242x217mm (144 x 144 DPI)

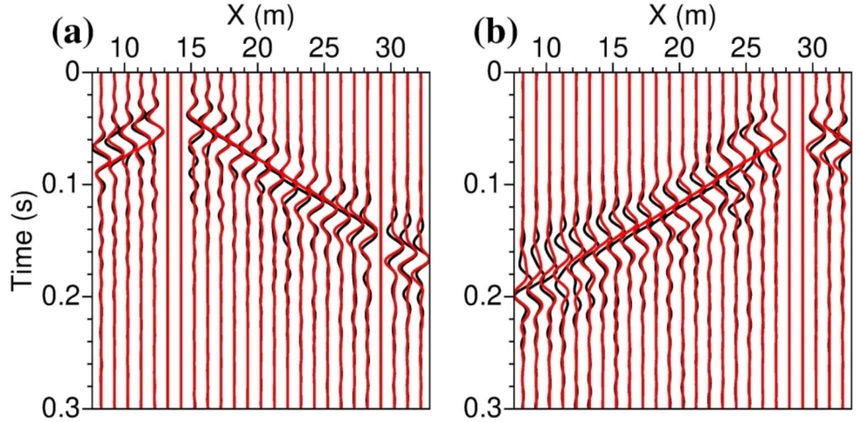

Figure 14: Comparison between measured (black) and modeled data (red) calculated using the inverted V_S model of Figure 12b. (a) The measured and modeled common-source gather with their sources located at x = 14.5 m along with line A. Data are bandlimited within the frequency range of $5 \sim 60$ Hz. Traces are normalized using the maximum value in each trace individually; only every fourth trace is displayed. (b) is the same as (a), but for a source at x = 29.5 m.

150x80mm (300 x 300 DPI)

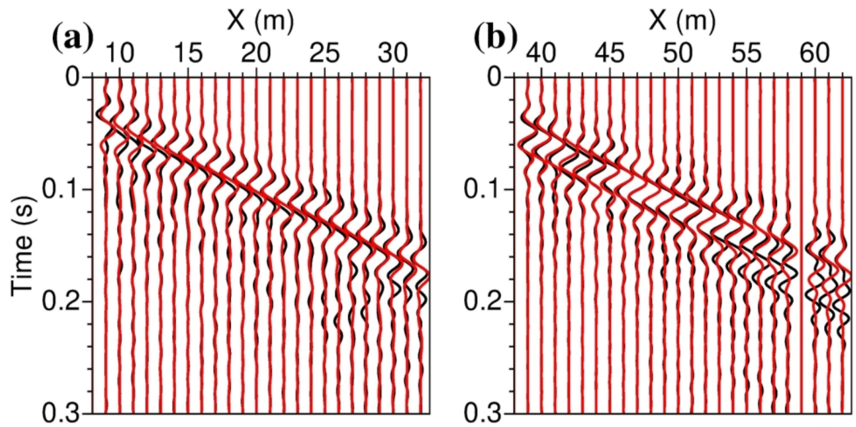

Figure 15: Same as in Figure 14, but for two common-source gathers acquired along seismic line B with lateral position of the source at x = 10.5, 40.5 m, respectively.

150x80mm (300 x 300 DPI)

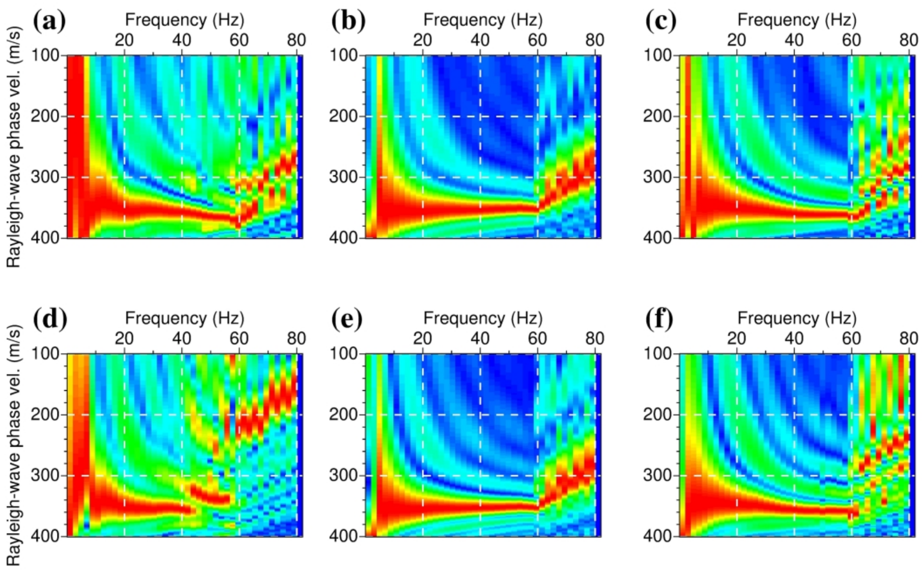

Figure 16: Comparison of Rayleigh-wave dispersion images for preprocessed field data, computed data from the initial model, and computed data from the inverted model. (a) Dispersion image calculated from the preprocessed common-source gather shown in Figure 14a, the source is located at x = 14.5 m; (b) dispersion image from the computed data using the initial model shown in Figure 12a; (c) dispersion image from the computed data using the inverted model shown in Figure 12b. (d), (e), (f) are same as (a), (b), (c) but for a common-source gather with the source located at x = 29.5 m.

241x146mm (300 x 300 DPI)

DOI:10.1190/geo2021-0467.1

DATA AND MATERIALS AVAILABILITY

Data associated with this research are available and can be obtained by contacting the corresponding author.

DOI:10.1190/geo2021-0467.1